

# Sim2Real Physically Informed Neural Controllers for Robotic Deployment of Deformable Linear Objects

Dezhong Tong<sup>1</sup>, Andrew Choi<sup>2</sup>, Longhui Qin<sup>1,5</sup>, Weicheng  
Huang<sup>1,5</sup>, Jungseock Joo<sup>3,4</sup>, and M. Khalid Jawed<sup>1</sup>

<sup>1</sup>*Department of Mechanical & Aerospace Engineering,  
University of California, Los Angeles, CA 90024, USA*

<sup>2</sup>*Department of Computer Science, University of California, Los Angeles, CA 90024, USA*

<sup>3</sup>*Department of Communications, University of California, Los Angeles, CA 90024, USA*

<sup>4</sup>*NVIDIA Corporation, Santa Clara, CA 95051, USA*

<sup>5</sup>*School of Mechanical Engineering, Southeast University, Nanjing 211189, China\**

## Abstract

Deformable linear objects, such as rods, cables, and ropes, play important roles in daily life. However, manipulation of DLOs is challenging as large geometrically nonlinear deformations may occur during the manipulation process. This problem is made even more difficult as the different deformation modes (e.g., stretching, bending, and twisting) may result in elastic instabilities during manipulation. In this paper, we formulate a physics-guided data-driven method to solve a challenging manipulation task – accurately deploying a DLO (an elastic rod) onto a rigid substrate along various prescribed patterns. Our framework combines machine learning, scaling analysis, and physics-based simulations to develop a physically informed neural controller for deployment. We explore the complex interplay between the gravitational and elastic energies of the manipulated DLO and obtain a control method for DLO deployment that is robust against friction and material properties. Out of the numerous geometrical and material properties of the rod and substrate, we show that only three non-dimensional parameters are needed to describe the deployment process with physical analysis. Therefore, the essence of the controlling law for the manipulation task can be constructed with a low-dimensional model, drastically increasing the computation speed. The effectiveness of our optimal control scheme is shown through a comprehensive robotic case study comparing against a heuristic control method for deploying rods for a wide variety of patterns. In addition to this, we also showcase the practicality of our control scheme by having a robot accomplish challenging high-level tasks such as mimicking human handwriting and tying knots.

## I. INTRODUCTION

Intelligent manipulation of deformable objects, such as ropes and cloth, is necessary for beneficial and ubiquitous robots. As most objects in the practical world are non-rigid, endowing robots with proper manipulation skills for deformable objects has humanitarian and economic potential. Some examples include robotic surgical suturing [33, 36], wire management [35], laundry folding [24], and caregiving for elderly and disabled communities [6, 7, 13, 29, 54]. However, given the large and geometrically nonlinear deformations of deformable objects, it is difficult to obtain an obvious mapping from the observations

---

\* khalidjm@seas.ucla.edu

of those manipulated objects to a concrete robotic manipulation scheme. Therefore, developing accurate and effective strategies for manipulating deformable objects is still an open research problem.

Among various deformable objects, deformable linear objects (DLOs), which includes elastic rods and the extensions of rods-like structures, e.g., cables, ropes, rods, and wires [31], have attracted significant research interest due to their widespread industrial and domestic applications. In this article, we focus on the category of rod-like structures and adopt the term DLO to refer to those solid elongated objects. DLOs usually possess extremely complicated nonlinearity due to the coupling of their multiple deformation modes: twisting, bending and stretching. Given the practicality and difficulty of manipulating DLOs, there is a growing need for robust and effective methods to manipulate DLOs.

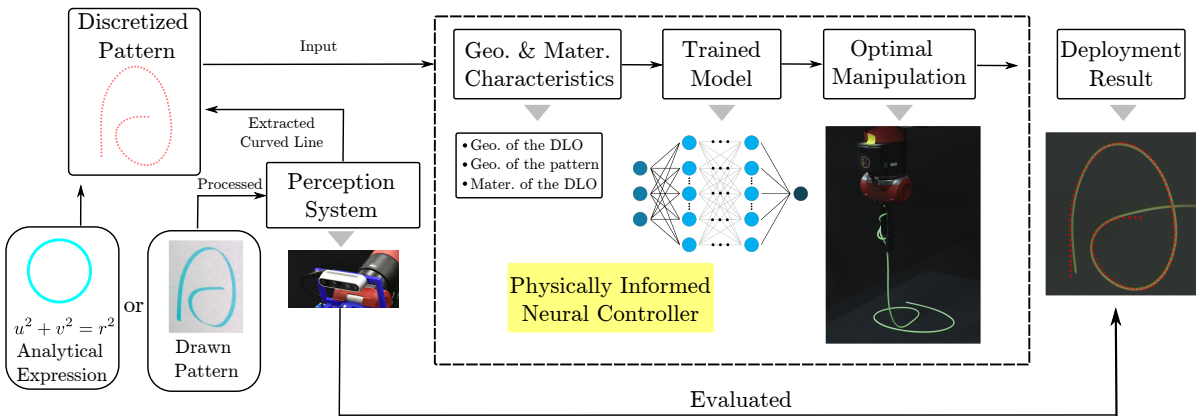


FIG. 1. A fully pipeline about deploying a DLO with a physically informed deployment scheme. The pipeline begins by discretizing the DLO pattern, which can be obtained through user input via an analytical expression or hand-drawn pattern. A physically informed neural controller then generates an optimal manipulation path for deploying the pattern, taking into account the shape of the pattern, as well as the geometrical and material properties of the DLO. Finally, the deployment result is evaluated using a perception system to assess the accuracy of the deployment.

Prior works on manipulating DLOs can be divided into two categories. The first involves robots attempting to manipulate DLOs to satisfy some high-level conditions without controlling the exact shapes of DLOs. This includes knot tangling/untangling [30, 48], obstacle avoidance [23, 25], following guidance and insertion [35, 55], etc. The second category in-

volves robots attempting to precisely control the exact shape of the DLOs. For this task, a key challenge is formulating a mapping between the robot's motions and the shape of the manipulated DLO [18, 27, 40]. In this article, we look into how to design a manipulation scheme for controlling the shape of elastic rods through deployment, which involves manipulating one end of DLO in a way that gradually lays the DLO on a substrate in a desired pattern, with superhuman accuracy, sufficient efficiency, and strong robustness. The fully pipeline of our physically informed deployment sceheme is shown in Fig. 1. In addition to achieving precise shape control, we show our control method can be used to solve high-level tasks such as reproducing human writing with a deployed DLO and knot tying.

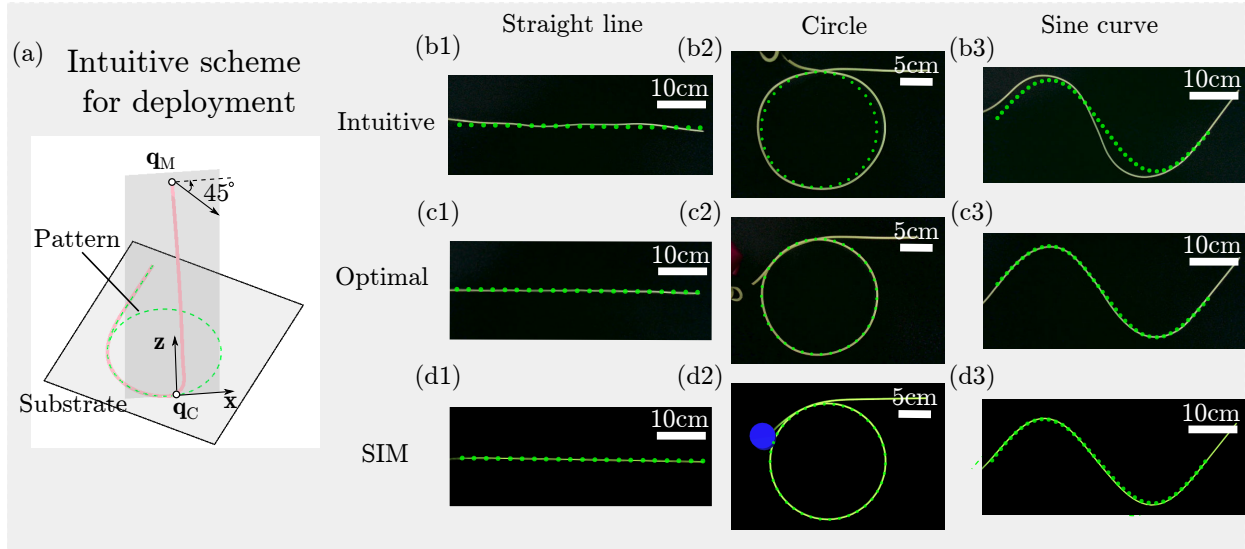


FIG. 2. Comparison of experimental results between the (b) intuitive control method, (c) our designed optimal control method, (d) and simulation results using the optimal control method for the patterns of straight line, circle, and sine curve. The schematic of the intuitive control method is shown in (a) and involves simply following the pattern while deploying.

### A. Deployment of DLOs

Deploying DLOs is instrumental in the practical world, e.g., drawing or writing on cakes with ice cream [38], deploying marine cables [50], depositing carbon nanotubes [8], and melting electrospinning for advanced manufacturing [42]. Therefore, a concrete and applicable deployment scheme is a perfect solution to the shape control problem of DLOs.

Now a natural question arises: how to deploy a DLO along a prescribed pattern accurately on the substrate? An intuitive method for deployment is shown in Fig. 2(a) where the manipulator grabs one end of the rod to move along a prescribed direction in the workspace. The direction is determined by rotating  $x$ -axis by an angle of 45 degrees about the negative  $z$ -axis, where both  $x$ -axis and  $z$ -axis are body-fixed axes attached on the connecting point  $\mathbf{q}_C$ :  $x$ -axis is along the tangent of the pattern at the connecting point  $\mathbf{q}_C$  and the  $z$ -axis is along the vertical direction, perpendicular to the rigid substrate. This direction is obtained with the common sense that the added deposited part length is presumed to be equal to the vertical displacement along the negative  $z$ -axis. A full description of the intuitive deployment scheme is stated in Alg. 1, where  $L$  is the total length of the rod for deployment;  $\mathbf{P}(s)$  is a prescribed pattern which evolves along the arc length  $s$  on the substrate,  $S$  is the total curve length of the pattern, and  $\mathbf{T}(s)$  is the tangent along the pattern. Note that  $\hat{()}$  indicates a unit vector in this article. Nevertheless, the robotic experimental results show that intuitive control methods cannot achieve good performance as shown in Fig. 2(b1-b3) as they do not consider the elasticity and geometric nonlinearity of the manipulated DLO.

In this paper, we propose a framework that combines physically accurate simulation, scaling analysis, and machine learning to generate an optimized control scheme capable of deploying solid rod-like structures, which we refer to as DLOs, along any feasible pattern. Our control scheme does not currently incorporate energy dissipation from manipulations with DLOs such as viscous threads, as our physical-based simulation is based on the rod model. However, the controlling scheme can be adapted by adjusting the physical-based simulation in our combined framework to include these factors. We validate the scheme with elastic rods, a canonical case of DLO made up of uniform isotropic linear elastic material, in robotic experiments. The usage of physically accurate numerical simulations not only allows us to incorporate physics into our manipulation scheme but also obtains full sim2real realization. Scaling analysis allows us to formulate the problem with generality using non-dimensional parameters, resulting in a control scheme robust against the material properties of the manipulated rods. Finally, machine learning allows us to train a neural network to model the controlling rules of deployment in a data-driven fashion. The high inference speed of our neural controller makes real-time operation feasible.

Our main contributions are as follows: (1) we formulate a solution to the DLO shape control problem through deployment with a physically robust scheme that leverages scaling

---

**Algorithm 1:** Intuitive Control Method

---

**Input:**  $L, \mathbf{P}$ **Output:**  $\tau$ **1 Func**  $\text{INT}(L, \mathbf{P})$ :

```
2    $\Delta s \leftarrow$  deployment rate
3    $\tau \leftarrow$  initialize an empty list
4    $s \leftarrow 0$ 
5    $\hat{\mathbf{z}} \leftarrow$  director along vertical direction
6    $S, \mathbf{T} \leftarrow \text{ProcessPattern}(\mathbf{P})$ 
7   while  $s \leq S$  do
8      $\mathbf{x}_C \leftarrow \mathbf{P}(s)$ 
9      $\hat{\mathbf{x}} \leftarrow \mathbf{T}(s)$ 
10     $\mathbf{q} \leftarrow \mathbf{P}(s) + (L - s)\hat{\mathbf{z}}$ 
11     $\mathbf{R} \leftarrow (\hat{\mathbf{x}}, \hat{\mathbf{z}} \times \hat{\mathbf{x}}, \hat{\mathbf{z}})$ 
12     $\tau.\text{append}((\mathbf{q}, \mathbf{R}))$ 
13     $s \leftarrow s + \Delta s$ 
14 return  $\tau$ 
```

---

analysis, resulting in generality against material, geometric, and environmental factors (friction); (2) we train a neural network with non-dimensional simulation data to serve as a fast and accurate neural controller for optimal manipulations of deployment; (3) we demonstrate full sim2real realization through an extensive robotic case study demonstrating our control method’s success for various practical deployment patterns, and (4) we showcase the utility of our control scheme for complex high-level applications such as mimicking human drawings for both deploying letters as well as to tie a trefoil knot.

## B. Overview

The remainder of the article is organized as follows: we begin with a literature review related to robotic DLO shape control in Sec. II. The formulation of the physics-based numerical model is discussed in Sec. III, where we also formulate the deployment problem

with scaling analysis. In Sec. IV, we analyze the nonlinearity of the deployment in detail and show how to discover the optimal manipulation actions with numerical simulation. In addition, a learning framework is formulated to obtain a fast, generalized motion planning solution. Next, in Sec. V, we introduce our overall robotic system, including perception and motion planning modules. Experimental results and analysis for different deployment cases, including writing letters and tying a knot, are given in Sec. VI. Finally, we provide concluding remarks and discuss the future research avenues in Sec. VII.

## II. RELATED WORK

Constructing the mapping relationship from the observations of manipulated DLOs to the robot’s action space is the primary basis of controlling DLOs. To uncover this mapping relationship, prior works usually implemented models to predict or perception systems to observe the deformations of DLOs under various manipulations. Manipulation schemes are then generated based on the predicted or sensed data. Therefore, model-based and perception-based methods can be considered two of the main categories for tackling manipulation problems of deformable objects. Due to the outstanding performance of machine learning algorithms for processing and generalizing data from models and perceptions, learning-based approaches have become another mainstream solution. In fact, many prior works take advantage of a combination of these three methods to develop hybrid schemes for different manipulation tasks. Here, we carry out a systematic review of prior scholarly contributions that have utilized techniques based on the three delineated categories to manipulate DLOs and other deformable objects.

Perception-based approaches involve utilizing sensors such as tactile sensors [35] and cameras [16, 21, 41, 51] to generate motions based on detected deformations. While sensors can capture the deformations as the manipulation proceeds, perception-based methods are usually not robust against the material and geometrical differences of the manipulated objects. In [41], a learning-based perception framework is presented based on the Coherent Point Drift algorithm, which is able to register states of manipulated DLOs with captured images. [51] developed state estimation algorithms for DLOs based on images so that a robot can do the following pick-and-place manipulation on the detected configuration of DLO. However, those perception systems based on cameras suffer from extracting accurate results when

occlusions happen. To overcome this shortcoming, tactile sensors have become prevalent in the robotics community. For example, [35] implements GelSight, a force feedback tactile sensor, to perform robotic cable management. Since sensing data by itself cannot predict future deformations of the manipulated objects, pure perception-based methods are typically insufficient for complex deformable material manipulation tasks.

Model-based methods usually construct a physically accurate model to predict the behavior of manipulated DLOs. Multiple methods exist for modeling DLOs [31, 52]. A simple and widely-used model, mass-spring systems are often used to model deformable objects including ropes [15, 20, 32], fabrics [9, 19], etc. However, due to the simplification of mass-spring systems, such models usually suffer from inaccuracies when undergoing large deformations and lack of physical interpretability. Position-based dynamics is another type of modeling method which usually represents DLOs as chains of rigid bodies [26, 34, 43] and introduces constraints between the positions of those rigid bodies to simulate deformations. Though this method is straightforward and fast, physical interpretability is also lacking.

Finite element methods (FEM) are also a popular avenue for modeling deformable objects [3, 10, 14]. However, FEM usually requires considerable computation resources and are hardly suitable for online predictions. More recently, fast simulation tools from the computer graphics community have attracted researchers' attention. For example, Discrete Elastic Rods (DER) [1, 2] has arisen as a robust and efficient algorithm for simulating flexible rods. [18] used DER as a predictive modeling tool, and achieved promising performance in DLO manipulation tasks. Though various ways to model deformable objects exists, each has their respective strengths and weaknesses and often possess a trade-off between computational efficiency and accuracy.

Finally, learning-based approaches have become prevalent as they are capable of not only predicting the shape of the deformable object but also higher-level information such as forces [47]. Most prior works use human demonstrations or robot explorations to train controlling policies for different tasks. [27], [39], and [17] fed human-made demonstrations to robots for learning control policies for shape control and knot-tying. Due to the tedium of constructing manual demonstrations, some researchers take advantage of the robots' automation to learn a policy purely from robotic exploration [49, 53]. To acquire training data more efficiently, researchers have also looked into training policies purely from simulation [22]. Although learning-based methods have shown promising performance for manipulating deformable

objects, the trained policies are often only valid for specific tasks whose state distribution matches that of the training set. In other words, learning-based approaches often fail when parameters such as the material and geometrical properties of the manipulated object change.

More relevant to the deployment task itself, [40] implemented the intuitive control method stated in Algo. 1 for controlling the shape of a rope to make a clove hitch knot. They achieve a success rate of 66% but require empirical hardcoded adjustments to their controlling scheme, indicating the intuitive approach’s unsuitability for extreme precision deployment. Additionally, [18] use a precise physical numerical model to predict the DLO’s configuration during deployment. However, they use a trial-and-error method to exhaustively solve the optimal deployment path, which is computationally expensive and slow.

Although the three discussed types of methods are suitable to be combined when solving deformable manipulation problems because of the complementary of their pros and cons, how to develop a combined approach to take advantage of different types of approaches is still an open problem in the robotic community. We find that combining physically accurate simulations and machine learning can endow the learned model with excellent accuracy from the simulations and real-time performance because of the inference speed of the neural network. In addition, scaled physics analysis, which is a vital tool from the mathematical physics community, is valuable for augmenting the model with high generality.

In this article, we show how a scaled physical analysis can extract the true contributing factors of the deployment problem and how a learning-based approach can generalize the information from physics to offer real-time computation speed for the manipulation task.

### III. NUMERICAL FRAMEWORK AND PHYSICAL ANALYSIS

In this section, we first discuss the numerical framework for studying the nonlinear behaviors of the DLO during deployment. Then, we extract the main controlling parameters for the analyzed system with the Buckingham- $\pi$  theorem.

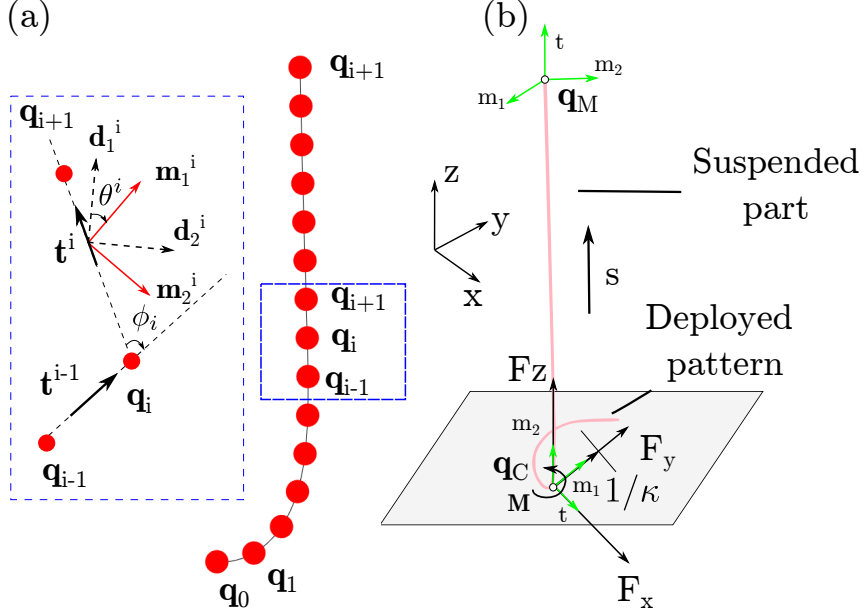


FIG. 3. (a) Discrete diagram of the centeline of a DLO and relevant notations; (b) schematic of deploying a DLO along a prescribed pattern.

### A. Discrete Differential Geometry (DDG)-based Numerical Framework

To simulate DLOs, we use a differential-discrete-geometry (DDG)-based simulator – Discrete Elastic Rods (DER) [1] – whose physical accuracy has been validated in many various scenarios such as flagella motions [12], knot tying [4, 45, 46], rod coiling [11], and elastic buckling in structures [44].

As shown in Fig. 3(a), the centerline of a DLO can be discretized into  $N + 1$  nodes  $[\mathbf{q}_0, \mathbf{q}_1, \dots, \mathbf{q}_N]$  ( $\mathbf{q}_i \in \mathbb{R}^3$ ) and  $N$  edges  $[\mathbf{e}^0, \mathbf{e}^1, \dots, \mathbf{e}^{N-1}]$  ( $\mathbf{e}^i = \mathbf{q}_i - \mathbf{q}_{i-1}$ ). In this section, subscripts correspond to node-relevant parameters, e.g.,  $\mathbf{q}_i$ , while superscripts correspond to edge-relevant parameters,  $\mathbf{e}^i$ . Each edge  $\mathbf{e}^i$  possesses two orthogonal frames: a reference frame  $[\mathbf{d}_1^i, \mathbf{d}_2^i, \mathbf{t}^i]$  and a material frame  $[\mathbf{m}_1^i, \mathbf{m}_2^i, \mathbf{t}^i]$ . The material frame, which captures the rotation of the centerline of the DLO, can be obtained from the reference frame and a rotation angle  $\theta^i$  between the two frames. The reference frame is predefined at the initial time  $t = 0$  and is updated between time steps using time parallel transport [1]. The following DOF vector of size  $(4N + 3)$  is constructed to capture all the deformations of the rod:

$$\mathbf{q} = [\mathbf{q}_0, \theta^0, \mathbf{q}_1, \dots, \mathbf{q}_{N-1}, \theta^{N-1}, \mathbf{q}_N]. \quad (1)$$

Indeed, the deformations of a DLO can be divided into three modes, each corresponding to a distinct type of elastic energy: stretching, bending, and twisting. Using the formulations of these elastic energies, we can outline the equations of motion (EOM) we must solve at each time step.

First, we write down the formulation of stretching energy:

$$E_s = \frac{k_s}{2} \sum_{i=0}^{N-1} \left( 1 - \frac{\|\mathbf{e}^i\|}{\|\tilde{\mathbf{e}}^i\|} \right)^2 \|\tilde{\mathbf{e}}^i\|, \quad (2)$$

where  $k_s$  is the stretching stiffness and  $\|\tilde{\mathbf{e}}^i\|$  is the undeformed length of the  $i$ -th edge. Note that we assume that the manipulated rod is of an isotropic linear elastic material in this project. Hereafter, all quantities with  $\tilde{}$  refer to their resting undeformed value.

Next, the bending energy is outlined as

$$E_b = k_b \sum_{i=1}^{N-1} \frac{\left( 2 \tan \frac{\phi_i}{2} - 2 \tan \frac{\tilde{\phi}_i}{2} \right)^2}{\|\tilde{\mathbf{e}}^i\| + \|\tilde{\mathbf{e}}^{i-1}\|}, \quad (3)$$

where  $k_b$  is the bending stiffness, and  $\phi_i$  is the turning angle at a node (as shown in Fig. 3(a)). Note that we also assume that the resting undeformed shape of the rod is straight, i.e.,  $\bar{\phi}_i = 0$  in our study.

Finally, the twisting energy is

$$E_t = k_t \sum_{i=1}^{N-1} \frac{\tau_i^2}{\|\tilde{\mathbf{e}}^i\| + \|\tilde{\mathbf{e}}^{i-1}\|}, \quad (4)$$

where  $k_t$  is the twisting stiffness,  $\tau_i = \theta_i - \theta_{i-1} + \Delta\tau_i^{\text{ref}}$  is the discrete twist, and  $\Delta\tau_i^{\text{ref}}$  is the angular difference between the reference frames on edges  $\mathbf{e}_{i-1}$  and  $\mathbf{e}_i$ .

With Eqs. 2, 3, and 4, the internal forces of the rod can be obtained as

$$\mathbf{F}^{\text{int}} = -\frac{\partial(E_s + E_b + E_t)}{\partial \mathbf{q}}. \quad (5)$$

We can then construct and solve the equations of motion implicitly based on Newton's second law:

$$\mathcal{R}(\mathbf{q}) \equiv \frac{\mathbb{M}}{\Delta t} \left( \frac{\mathbf{q}(t_{i+1}) - \mathbf{q}(t_i)}{\Delta t} - \dot{\mathbf{q}}(t_i) \right) - \mathbf{F}^{\text{int}} - \mathbf{F}^{\text{ext}} = 0, \quad (6a)$$

$$\dot{\mathbf{q}}(t_{i+1}) = \frac{\mathbf{q}(t_{i+1}) - \mathbf{q}(t_i)}{\Delta t}, \quad (6b)$$

where  $\mathbb{M}$  is a square lumped mass matrix of size  $4N + 3$ ;  $\mathbf{F}^{\text{int}}$  is a  $(4N + 3) \times 1$  elastic force vector (from Eq. 5), and  $\mathbf{F}^{\text{ext}}$  is a  $(4N + 3) \times 1$  external force vector. The  $(\cdot)$  decorator represents the derivative of a quantity with respect to time, i.e.,  $\dot{\mathbf{q}}(t_i)$  is the velocity vector at time  $t_i$ . Note that the subscript in Eq. 6 is the time stamp. By solving Eq. 6 with Newton's method, the mechanical deformation of the manipulated rod over time can be simulated accurately.

## B. Physical Analysis and Controlling Rule Construction

As shown in Fig. 3(b), when a DLO is deployed along a substrate, it can be divided into two parts: a deployed and suspended part. Since the deployed part should be static during the remainder of the deployment, we focus primarily on the suspended part.

Before analyzing the system, we first introduce some quantities to assist our analysis. Here, we define an arc length  $s$  along the tangent of the suspended part so that the position of the node  $\mathbf{q}(s)$  is a function of  $s$ . For example, the connective node  $\mathbf{q}_C$ , which connects the deployed and suspended parts, can be expressed as  $\mathbf{q}_C = \mathbf{q}(0)$  while the manipulated node is  $\mathbf{q}_M = \mathbf{q}(l_s)$ , where  $l_s$  is the total arc length of the suspended part. Note that there is also a material frame  $\mathbf{m}(s) = [\mathbf{m}_1, \mathbf{m}_2, \mathbf{t}] \in SO(3)$  attached along the DLO to express the rotation along the DLO. With the help of  $\mathbf{q}(s)$  and  $\mathbf{m}(s)$ , the configuration of the suspended part can be fully described.

Eq. 6 implies that the DLO's configuration  $\mathbf{q}(s)$  and  $\mathbf{m}(s)$  can be solved when boundary conditions are determined. For the suspended part, the two key boundary conditions are the connective node  $\mathbf{q}_C$  and the manipulated node  $\mathbf{q}_M$ , as shown in Fig. 3(b). Since the deployed pattern is known, the boundary conditions at the connective node  $\mathbf{q}_C$  are also known. By inducing the boundary conditions at the manipulated end  $\mathbf{q}_M$ , we can then solve the configurations of the suspended part as follows:

$$\begin{aligned} \mathcal{R}(\mathbf{q}) &= 0, \\ \text{s.t. } \mathbf{q}(l_s) &= \mathbf{q}_M, \quad \mathbf{R} = \mathbf{m}(l_s)\mathbf{m}(0)^T, \\ \mathbf{q}(0) &= \mathbf{q}_C, \quad \frac{d\mathbf{q}(0)}{ds} = \mathbf{t}(0), \quad \frac{d\mathbf{t}(0)}{ds} = \kappa\mathbf{n}, \end{aligned} \tag{7}$$

where  $\mathbf{q}_M$  is the position and  $\mathbf{R}$ , which is the rotation from the connective node to the manipulated end, is the orientation of the manipulated end. Note that the position of the

connective node  $\mathbf{q}_C$ , tangent  $\mathbf{t}(0)$ , and curvature normal vector  $\kappa\mathbf{n}$  can be determined from the deployed pattern, where  $\mathbf{n}$  is the unit vector of the curvature direction in the x-y plane ( $\mathbf{n}$  is  $\hat{\mathbf{y}}$  in Fig. 3(b)). By solving Eq. 7, we can obtain the configuration of the suspended part for any predefined pattern and manipulated end pose.

Once the deformed configuration is known, we can then calculate the interaction responses between the rod and the substrate. To do so, we denote the external forces  $\mathbf{F}^{\text{ext}} = F_x\hat{\mathbf{x}} + F_y\hat{\mathbf{y}} + F_z\hat{\mathbf{z}}$  and twisting moment  $\mathbf{M}(0)$  applied on the connective node  $\mathbf{q}_C$ . Note that the moment  $\mathbf{M}$  is a function of arc length  $s$ , and  $\mathbf{M}(l_s)$  is the twisting moment applied on the manipulated end. The quantities  $\mathbf{F}^{\text{ext}}$  and  $\mathbf{M}(0)$  are relevant with the friction coefficient between the substrate and the rod, which is an unknown factor. Such uncertain influences must be eliminated when designing controlling rules. Furthermore, the manipulation end  $\mathbf{q}(l_s)$  should not have large deformations during the manipulation. To do so, we make the curvature (bending deformations) at the manipulated end to be 0 during the design of the manipulation scheme. Therefore, an optimization problem can be formulated to compute the optimal grasp of the manipulated end.

$$\begin{aligned} (\mathbf{q}_M, \mathbf{R}) &= \arg \min \left( \|\mathbf{F}^{\text{ext}}\|^2 + \left( \frac{\|\mathbf{M}(0)\|}{h} \right)^2 \right) \\ \text{s.t. } \frac{d\mathbf{q}(0)}{ds} &= \mathbf{t}(0), \quad \frac{d\mathbf{t}(0)}{ds} = \kappa\mathbf{n}, \quad \frac{d^2\mathbf{q}(l_s)}{ds^2} = 0 \end{aligned} \quad (8)$$

By solving Eqs. 7 and 8, we can obtain the optimal  $\mathbf{q}_M$  and  $\mathbf{R}$ . Therefore, a mapping relationship exists between all of the contributing factors of this system. Recall that in Eqs. 2, 3, and 4, stretching stiffness  $k_s$ , bending stiffness  $k_b$ , twisting stiffness  $k_t$ , density  $\rho$ , and rod radius  $h$  are the primary material and geometric properties of a rod. Adding in the geometrical properties, which is suspended length  $l_s$  and curvature  $\kappa$  at the connective node, of the deformed configuration of a deploying DLO, the following mapping relationship

$$(\mathbf{q}_M, \mathbf{R}) = f(l_s, \kappa, k_s, k_b, k_t, h, \rho), \quad (9)$$

can be constructed where  $f$  is a highly nonlinear (and unknown) function that describes the controlling rule. However, Eq. 9 is not unit-independent, which results in  $f$  having relatively high input dimensionality. Using Buckingham  $\pi$  theorem, we can convert the relationship

$f(\cdot)$  to the reduced-order non-dimensionalized form

$$\begin{aligned}
(\bar{\mathbf{q}}_M, \mathbf{R}) &= \mathcal{F}(\bar{l}_s, \bar{\kappa}, \bar{k}_s), \\
L_{gb} &= \left( \frac{k_b}{2\pi h^2 \rho g} \right)^{1/3}, \\
\bar{k}_s &= \frac{k_s L_{gb}^2}{k_b}, \\
\bar{\mathbf{q}}_M &= \frac{\mathbf{q}_M - \mathbf{q}_C}{L_{gb}}, \\
\bar{l}_s &= \frac{l_s}{L_{gb}}, \\
\bar{\kappa} &= \kappa L_{gb}.
\end{aligned} \tag{10}$$

Hereafter, all quantities with  $(\bar{\cdot})$  indicate normalized quantities. Note that in Eq. 10, we do not consider the influence of the twisting stiffness  $k_t$  in this article, since twisting strains are minimal compared to bending and stretching. However, the influence of  $k_t$  can be also analyzed with our proposed analysis. In the following article, we will show how to establish the nonlinear function in Eq. 10.

#### IV. OPTIMIZATION AND DEEP LEARNING

In this section, we further analyze the optimization of the system to obtain the nonlinear mapping function in Eq. 10. Given the high nonlinearity of the system, we first solve Eq. 10 in a data-driven way through simulations. While doing so, we analyze the elastic instability of the system to choose the optimal of the deploying rule. Afterward, we reconstruct Eq. 10 using a neural network. This neural controller is then used by our robotic system as the controlling law to complete various deployment tasks in Sec. VI.

##### A. Elastic Instability in Deployment along a Straight Line

When a DLO is deployed along a straight line using the intuitive control method, only 2D deformations of the DLO should occur as manipulation is occurring in a 2D workspace. However, one intriguing phenomena is the failure case shown in Fig. 2(b1-b3), where intuitive deployment for a straight line will actually result in a curved line. This observation goes against our intuition and implies that there exists elastic instability during the intuitive deployment for a straight line.

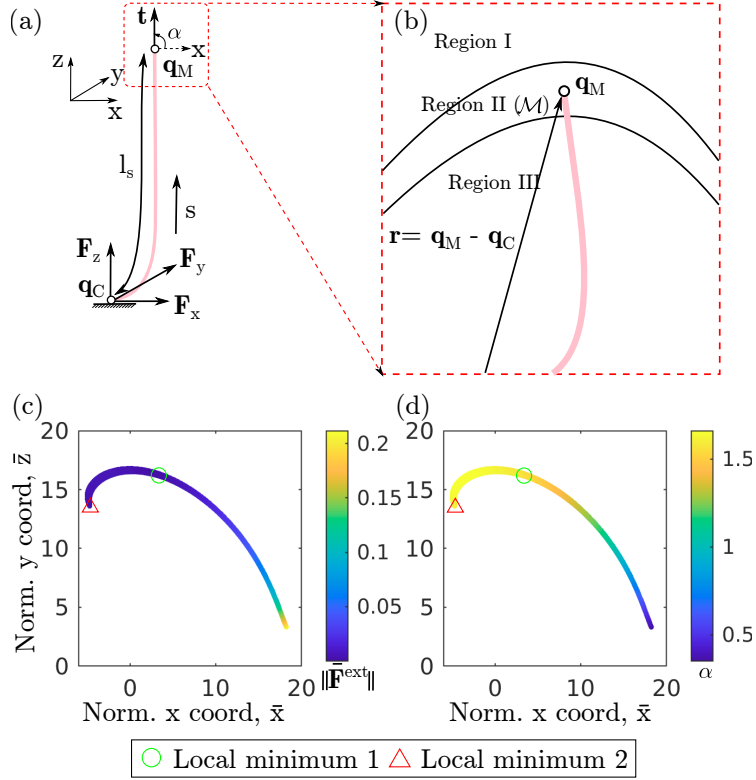


FIG. 4. Schematic of a rod manipulated in 2D workspace (a) and its available region  $\mathcal{M}$ ; visualization of the force  $\|\bar{\mathbf{F}}_x\|$  and orientation angle  $\alpha$  of the manifold  $\mathcal{M}$  when  $\bar{l}_s = 17.68$ .

As mentioned before, since the configuration of the deployed part is fixed, unknown deformations can only occur along the suspended part. When deploying a straight line on the substrate, the main deformations of the DLO should be within the  $x$ - $z$  plane as shown in Fig. 4(a). Given the suspended part's geometric properties and external forces, we can write down the constraints  $\mathcal{C}$  which should be satisfied:

$$\begin{aligned} \bar{\mathbf{q}}(\bar{s}) \cdot \hat{\mathbf{z}} &\geq 0 \quad \forall \bar{s} \in [0, \bar{l}_s], \\ \bar{\mathbf{F}}^{\text{ext}} \cdot \hat{\mathbf{z}} &\geq 0. \end{aligned} \quad (11)$$

These constraints enforce that (i) the suspended part should be above the substrate and (ii) external contact responses along the  $z$ -axis should always be larger than or equal to 0.

By solving Eq. 7 with the constraints  $\mathcal{C}$ , all potential poses of the manipulated end, which constitute a closed manifold  $\mathcal{M}$  for a fixed suspended length  $l_s$ , can be obtained. Note that the boundary condition at the connective node  $\bar{\mathbf{q}}_C$  is  $\mathbf{t}(0) = (1, 0, 0)$  and  $\bar{\kappa} = 0$  here. Each point in the manifold  $\mathcal{M}$  corresponds to a position  $\bar{\mathbf{q}}_M$  and rotation  $\mathbf{R}$  of the manipulated

end. Given that the deformed configuration is located within the 2D  $x$ - $z$  plane, we can use a  $2 \times 1$  vector  $\bar{\mathbf{q}}_M = (\bar{x}_{\text{Top}}, \bar{z}_{\text{Top}})$  to express the position of  $\bar{\mathbf{q}}_M$  and a scalar value  $\alpha$  to denote the rotation information. For example, tangent  $\mathbf{t}(\bar{l}_s) = (\cos(\alpha), \sin(\alpha))$  as shown in Fig. 4(a). Since the manifold  $\mathcal{M}$  is a closed set, all we need to obtain is the boundary of the manifold  $\partial\mathcal{M}$ . To discover the boundary  $\partial\mathcal{M}$ , we explore along a ray  $\mathbf{r}$  from the connective node  $\bar{\mathbf{q}}_C$  to the manipulated node  $\bar{\mathbf{q}}_M$ . This exploring ray can be divided into three distinct regions as shown in Fig. 4(b). When the manipulated end  $\bar{\mathbf{q}}_M$  exists in region I, the external force  $\bar{F}_z = F_z h^2/k_b$  must be smaller than 0 as stretching occurs, therefore violating the constraints  $\mathcal{C}$ . Furthermore, in region III, the manipulated end is too low causing  $\bar{l}_s$  to decrease past its intended value, which also violates the constraints  $\mathcal{C}$ . Therefore, the region  $\mathcal{M}$  that satisfies the constraints  $\mathcal{C}$  is region II, which exists between Regions I and III. In this article, we implement a bisection method to obtain the boundary of region II  $\partial\mathcal{M}$ . The pseudocode for the bisection method is given in Alg. 43.

Note that  $\theta$  in Alg. 43 is the angle between the  $x$ -axis and ray  $\mathbf{r}$ . Once the manifold  $\mathcal{M}$  is obtained, we can check the response forces for different poses in this manifold. A specific case for  $\bar{l}_s = 17.68$  is visualized in Fig. 4(c). Since deformations only occur in the  $x$ - $z$  plane, the twisting moment  $\bar{\mathbf{M}}(0) = \mathbf{M}(0)h/k_b$  applied on the connective node  $\bar{\mathbf{q}}_C$  is always 0. To achieve the optimal pose of the manipulated end for  $\bar{l}_s = 17.68$ , we need to find the poses in  $\mathcal{M}$  that minimize  $\|\bar{\mathbf{F}}^{\text{ext}}\|$ . In the case shown in Fig. 4(b), two local minima are found. However, not all of those correspond to the stable equilibrium, and the minimum with elastic stability is the optimum point. We can do so by carrying out a stability analysis.

To test the elastic stability of these two local minima, we apply a disturbance  $\Delta\bar{y} = y/L_{gb}$  along the  $y$ -axis while the manipulated end  $\bar{\mathbf{q}}_M$  is located at each local minimum. Fig. 5 shows both the change of  $\bar{F}_y = F_y h^2/k_b$  and configuration given this perturbation for each local optima. For local minimum 2, we can see a sudden snapping process, while the disturbance on local minimum 1 results in a continuous and steady change. Therefore, we can conclude that the optimum for deploying the DLO is at local minimum 1 since this minimum corresponds to a configuration with more gentle bending deformations of the suspended part. In other words, the neighboring region of local minimum 2 is more likely to encounter instability. Using the method introduced in this section, we can now output the optimal deployment rule for a straight line. The optima for straight-line deployment can be regarded as a seed to explore the optima for

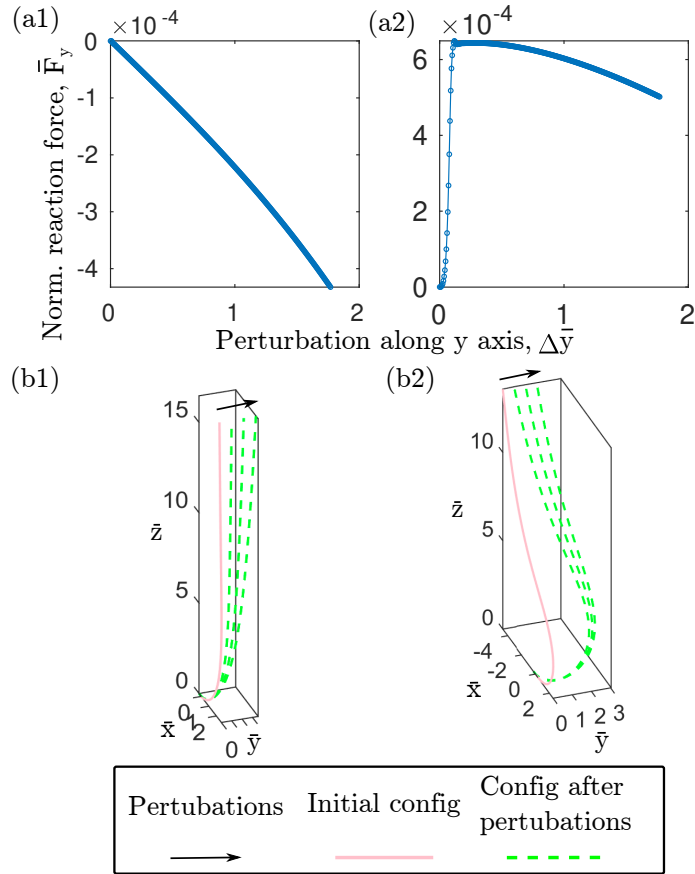


FIG. 5. Change of the magnitude of force  $F_y$  when adding a perturbation along the  $y$ -axis at local minimum 1 (a1) and local minimum 2 (a2), and change of the configurations of the rod when adding the perturbations at local minimum 1 (b1) and local minimum 2 (b2) for  $\bar{l}_s = 17.68$ .

more complex patterns. The next section discusses how to obtain the optima for deploying a DLO along any arbitrary prescribed pattern.

## B. Deployment in 3D Workspace

As mentioned in Sec. III B, the mapping relationship  $\mathcal{F}(\cdot)$  in Eq. 10 must be constructed to achieve optimal deployment in 3D workspace. For the connective node for any prescribed pattern, since the deformations of the pattern are only in the  $x$ - $y$  plane, we can ensure that the twisting moment  $\mathbf{M}(0)$  can always be 0. Therefore, the optimal pose of the manipulated

end can be obtained by minimizing  $\|\bar{\mathbf{F}}^{\text{ext}}\|$  by solving

$$\nabla_{\bar{\mathbf{q}}_M} \|\bar{\mathbf{F}}^{\text{ext}}\| = \frac{\partial \bar{\mathbf{F}}^{\text{ext}}}{\partial \bar{\mathbf{q}}_M} \bar{\mathbf{F}}^{\text{ext}} = 0. \quad (12)$$

As the deploying rod is a continuous system,  $\bar{\mathbf{F}}^{\text{ext}}$  must change when  $\mathbf{q}_M$  changes. Therefore, we can convert Eq. 12 to be a root finding problem

$$\bar{\mathbf{F}}^{\text{ext}} = 0. \quad (13)$$

---

**Algorithm 2:** Bisection Method for Obtaining  $\partial\mathcal{M}$

---

**Input:**  $\bar{l}_s, \bar{k}_s, \nu$

**Output:**  $\partial\mathcal{M}$

```

1 Func DiscoverManifoldBoundary( $\bar{l}_s, \bar{k}_s$ ):
2    $\theta \leftarrow$  a small positive value
3    $\beta \leftarrow$  a small positive value
4    $\partial M \leftarrow$  initialize an empty list
5    $\delta \leftarrow$  a small positive value as tolerance
6    $\mathbf{r}_c \leftarrow (\bar{l}_s \cos(\theta), \bar{l}_s \sin(\theta))$ 
7    $\mathbf{r}_f \leftarrow (0, 0)$ 
8    $\mathcal{R} \leftarrow$  initialized rod solver with  $\bar{l}_s, \bar{k}_s, \nu$ 
9   while  $\theta \leq \pi$  do
10    |  $\mathbf{r} \leftarrow \mathbf{r}_c$ 
11    | do
12    |   |  $\mathbf{r} \leftarrow (1 + \beta)\mathbf{r}$ 
13    |   |  $\bar{F}_z \leftarrow \mathcal{R}(\mathbf{r})$ 
14    | while  $\bar{F}_z < 0$ 
15    |   | while  $\mathcal{C}$  is not satisfied do
16    |   |   |  $\mathbf{r} \leftarrow \mathbf{r} - \delta \hat{\mathbf{r}}$ 
17    |   |   |  $\bar{\mathbf{q}}, \bar{F}_z \leftarrow \mathcal{R}(\mathbf{r})$ 
18    |   |   | if  $\|\mathbf{r}\| < 0$  then
19    |   |   |   | break
20    |  $\mathbf{r}_f \leftarrow \mathbf{r}$ 

```

---

---



---

```

22
23
24     while  $\|\mathbf{r}_c - \mathbf{r}_f\| \geq \delta$  do
25          $\bar{\mathbf{q}}, \bar{F}_z \leftarrow \mathcal{R}(\mathbf{r})$ 
26         if  $\mathcal{C}$  is satisfied then
27              $\mathbf{r}_f \leftarrow \mathbf{r}$ 
28         else
29              $\mathbf{r}_c \leftarrow \mathbf{r}$ 
30              $\mathbf{r} \leftarrow (\mathbf{r}_c + \mathbf{r}_f)/2$ 
31              $\partial\mathcal{M}.\text{append}((\mathbf{r} \cos \theta, \mathbf{r} \sin \theta))$ 
32              $\mathbf{r}_c \leftarrow \mathbf{r}$ 
33              $\mathbf{r}_f \leftarrow (0, 0)$ 
34             while  $\|\mathbf{r}_c - \mathbf{r}_f\| \geq \delta$  do
35                  $\bar{\mathbf{q}}, \bar{F}_z \leftarrow \mathcal{R}(\mathbf{r})$ 
36                 if  $\mathcal{C}$  is satisfied then
37                      $\mathbf{r}_c \leftarrow \mathbf{r}$ 
38                 else
39                      $\mathbf{r}_f \leftarrow \mathbf{r}$ 
40                      $\mathbf{r} \leftarrow (\mathbf{r}_c + \mathbf{r}_f)/2$ 
41                      $\partial\mathcal{M}.\text{append}((\mathbf{r} \cos \theta, \mathbf{r} \sin \theta))$ 
42                      $\theta \leftarrow \theta + \delta\theta$ 
43     return  $\partial\mathcal{M}$ 

```

---

As discussed before, solving the configurations of the deploying DLO is a boundary value problem. Since the boundary conditions on the connective end are constant, the external forces  $\bar{\mathbf{F}}^{\text{ext}}$  are influenced solely by the manipulated end pose  $\mathbf{q}_M$ , with a unique corresponding  $\mathbf{R}$  for describing the rotation of the manipulated end.

Given the high nonlinearity of the DLO, it is nontrivial to solve the root-finding problem in Eq. 13 analytically. Therefore, we employ a finite difference approach to calculate the numerical Jacobian of  $\mathbf{F}^{\text{ext}}$ . We perturb the manipulated end along  $x$ ,  $y$ , and  $z$ -axes with a

○ Simulation Data ■ Data from NN

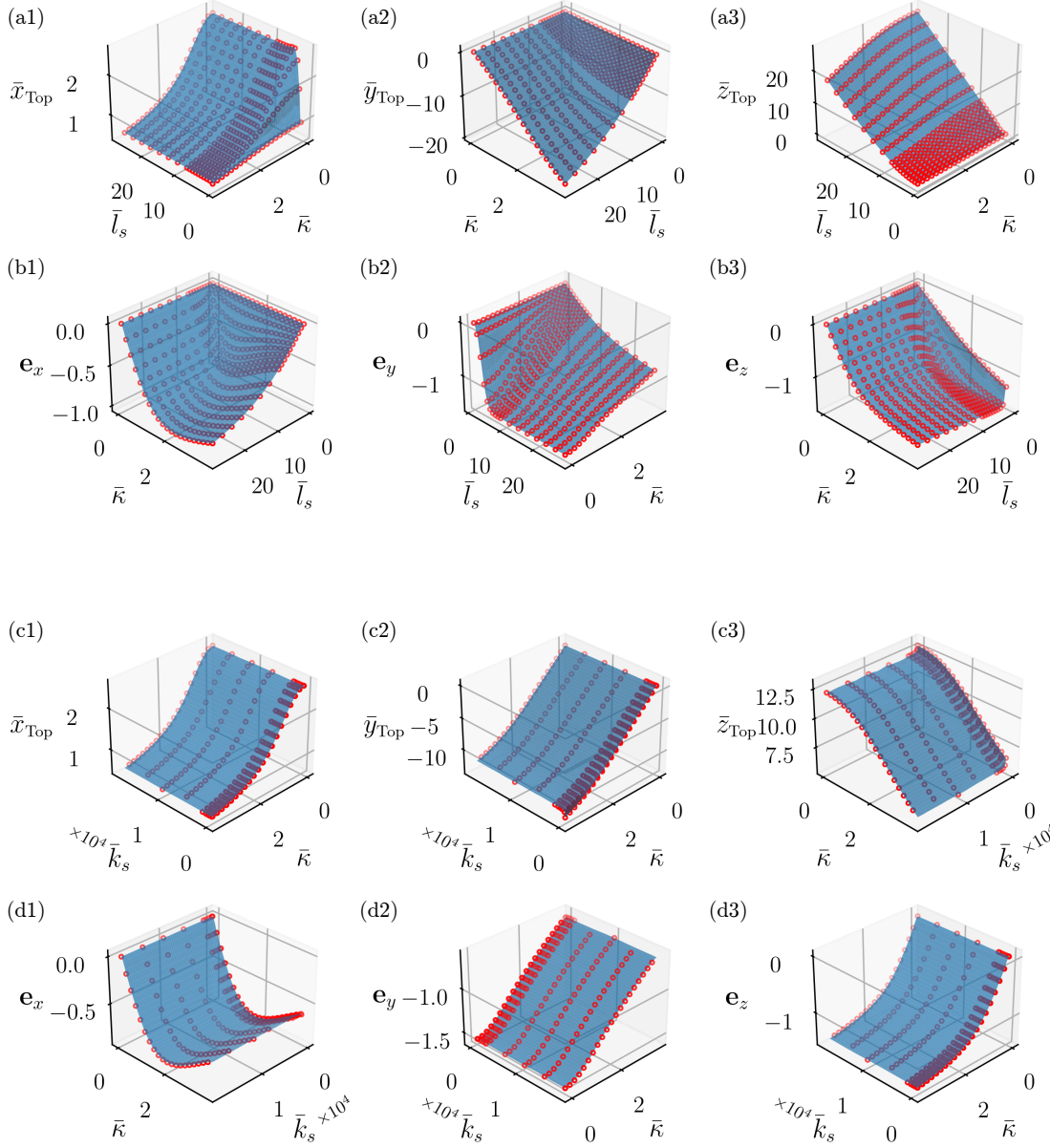


FIG. 6. Visualization of the influence from curvature  $\bar{\kappa}$  and suspended length  $\bar{l}_s$  on the (a1-a3) manipulated end position and (b1-b3) manipulated end orientation for fixed values of  $\bar{k}_s = 2087$ ; visualization of the influence from stretching stiffness  $\bar{k}_s$  and curvature  $\bar{\kappa}$  on the (c1-c3) manipulated end position and (d1-d3) manipulated end orientation with fixed values of  $\bar{l}_s = 13.68$ .

---

**Algorithm 3:** Gradient Descent for Optimal Grasp

---

**Input:**  $\bar{l}_s, \bar{\kappa}\mathbf{n}, \bar{k}_s, \nu$

**Output:**  $\bar{\mathbf{q}}_M^*$

1 **Func** OptimalGrasp( $\bar{l}_s, \bar{\kappa}, \bar{k}_s$ ):

2      $k \leftarrow 0$

3      $\delta \leftarrow$  a small value as tolerance

4      $\bar{\mathbf{q}}_M^{(k)} \leftarrow$  initialize a random pose of end-effector

5      $\mathcal{R}(\cdot) \leftarrow$  initialize the rod solver with  $\bar{l}_s, \bar{\kappa}, \bar{k}_s$

6     **do**

7          $\bar{\mathbf{F}}^{\text{ext}} \leftarrow \mathcal{R}(\bar{\mathbf{q}}_M^{(k)})$

8          $\mathbf{J}^{\text{ext}} \leftarrow$  Eq. 14

9          $\Delta\bar{\mathbf{q}} \leftarrow (\mathbf{J}^{\text{ext}})^{-1}\bar{\mathbf{F}}^{\text{ext}}$

10         $\alpha \leftarrow \text{LineSearch}(\bar{\mathbf{q}}_M^{(k)}, \Delta\bar{\mathbf{q}}, \|\bar{\mathbf{F}}^{\text{ext}}\|, \mathcal{R})$

11         $\bar{\mathbf{q}}_M^{(k+1)} \leftarrow \bar{\mathbf{q}}_M^{(k)} - \alpha\Delta\bar{\mathbf{q}}$

12         $k \leftarrow k + 1$

13     **while**  $\|\bar{\mathbf{F}}^{\text{ext}}\| \geq \delta$

14      $\bar{\mathbf{q}}_M^* \leftarrow \bar{\mathbf{q}}_M^{(k)}$

15     **return**  $\bar{\mathbf{q}}_M^*$

---

small distance  $\delta$  and use the finite difference to compute the numerical Jacobian:

$$\mathbf{J}^{\text{ext}} = \begin{bmatrix} \frac{\bar{\mathbf{F}}^{\text{ext}}(\bar{\mathbf{q}}_M + \delta\hat{\mathbf{x}}) - \bar{\mathbf{F}}^{\text{ext}}(\bar{\mathbf{q}}_M)}{\delta}, \\ \frac{\bar{\mathbf{F}}^{\text{ext}}(\bar{\mathbf{q}}_M + \delta\hat{\mathbf{y}}) - \bar{\mathbf{F}}^{\text{ext}}(\bar{\mathbf{q}}_M)}{\delta}, \\ \frac{\bar{\mathbf{F}}^{\text{ext}}(\bar{\mathbf{q}}_M + \delta\hat{\mathbf{z}}) - \bar{\mathbf{F}}^{\text{ext}}(\bar{\mathbf{q}}_M)}{\delta} \end{bmatrix}^T, \quad (14)$$

where  $T$  is the transpose operator and  $\delta\hat{\mathbf{x}}, \delta\hat{\mathbf{y}}$ , and  $\delta\hat{\mathbf{z}}$  are small perturbations along  $x$ ,  $y$ , and  $z$ -axes, respectively, i.e.,  $\delta\hat{\mathbf{x}} = [\delta, 0, 0]^T$ .

Here,  $\mathbf{J}^{\text{ext}}$  is a  $3 \times 3$  matrix and can be used to calculate the Newton search step so that Eq. 13 can be solved with a gradient descent method. Further details of this solving process are stated in Alg. 3. Additionally, we also implement a line search algorithm to help determine the appropriate step size for the Newton search step  $\Delta\bar{\mathbf{q}}$  as shown in Alg. 4.

In this article, both position  $\bar{\mathbf{q}}_M$  and rotation  $\mathbf{e}$  of the manipulated end are represented as  $3 \times 1$  vectors:  $\bar{\mathbf{q}}_M = (\bar{x}^{\text{Top}}, \bar{y}^{\text{Top}}, \bar{z}^{\text{Top}})$  and  $\mathbf{e} = (e_x, e_y, e_z)$ . The rotation vector  $\mathbf{e}$  can

---

**Algorithm 4:** Line Search Algorithm

---

**Input:**  $\bar{\mathbf{q}}_M, \Delta\mathbf{q}, f_0, \mathcal{R}$

**Output:**  $\alpha$

```

1 Func LineSearch( $\bar{\mathbf{q}}_M, \Delta\mathbf{q}, f_0, \mathcal{R}, \alpha_0 = 1, m = 0.5$ ):
2    $\alpha \leftarrow \alpha_0$ 
3    $k \leftarrow 0$ 
4   success  $\leftarrow$  False
5   do
6      $\bar{\mathbf{q}}_M^{(k)} \leftarrow \bar{\mathbf{q}}_M - \alpha \Delta\mathbf{q}$ 
7      $\bar{\mathbf{F}}^{\text{ext}} \leftarrow \mathcal{R}(\bar{\mathbf{q}}_M^{(k)})$ 
8      $f^{(k)} \leftarrow \|\bar{\mathbf{F}}^{\text{ext}}\|$ 
9     if  $f^{(k)} \geq f_0$  then
10       $\alpha = m\alpha$ 
11       $k \leftarrow k + 1$ 
12    else
13      success  $\leftarrow$  True
14  while not success
15  return  $\alpha$ 

```

---

be translated to a rotation matrix through an axis-angle representation  $(\hat{\mathbf{e}}, \|\mathbf{e}\|)$ , where  $\|\mathbf{e}\|$  is the rotation angle along the rotation axis  $\hat{\mathbf{e}} = \mathbf{e}/\|\mathbf{e}\|$ . For an input tuple  $(\bar{l}_s, \bar{\kappa}, \bar{k}_s)$ , we can now solve for the optimal pose of the manipulated end  $(\mathbf{q}_M^*, \mathbf{e}^*)$ . Visualizations of the discretely solved optimal poses obtained from simulation are shown as red hollow circles in Fig. 6.

We now know how to obtain the optimal manipulation pose given the input  $(\bar{l}_s, \bar{\kappa}, \bar{k}_s)$  with simulations. However, solving for the optimal poses through the simulation make real-time manipulation infeasible. Instead, the following section introduces using a neural network to learn the optimal controlling rule for fast real-time inference.

### C. Training the Neural Controller

Rather than obtaining solutions for  $\mathcal{F}$  through endless simulations, we train a neural network to obtain an analytical approximation of  $\mathcal{F}$  similar to [47]. We use a simple fully-connected feed-forward nonlinear regression network consisting of 4 hidden layers, each with 392 nodes, as the network architecture. Aside from the output, each layer is followed by a rectified linear unit (ReLU) activation.

We frame the neural controller to have an input  $\mathbf{i} \in \mathbb{R}^3$  and an output  $\mathbf{o} \in \mathbb{R}^6$ , where the input consists of the 3 non-dimensional values  $\bar{l}_s$ ,  $\bar{\kappa}$ , and  $\bar{k}_s$  and the output consists of two concatenated  $3 \times 1$  vectors: the optimal position  $\bar{\mathbf{q}}_M$  and rotation  $\mathbf{e}$  of the manipulated end. Using our simulation framework, we construct a dataset  $\mathcal{D}$  consisting of 6358 training samples.

When training the neural controller, we first preprocess all inputs  $\mathbf{i}$  through the standardization

$$\mathbf{i}' = \frac{\mathbf{i} - \bar{\mathbf{i}}_{\mathcal{D}}}{\sigma_{\mathcal{D}}},$$

where  $\bar{\mathbf{i}}_{\mathcal{D}}$  and  $\sigma_{\mathcal{D}}$  are the mean and standard deviation of the input portion of the dataset  $\mathcal{D}$ . Afterwards, we use an initial 80-20 train-val split on the dataset  $\mathcal{D}$  with a batch size of 128. We use mean absolute error (MAE) as our loss and use a training strategy that alternates between stochastic gradient descent (SGD) and Adam whenever training stalls. In addition, the batch size is gradually increased up to a max size of 2048 and the entire dataset is used to train the controller once MAE reaches  $< 0.003$ . With this scheme, we achieve a final MAE of  $< 0.0015$ .

## V. ROBOTIC SYSTEM

### A. Perception System

To obtain the Cartesian centerline coordinates of the deployed DLO (or drawn patterns), we use the DLO perception algorithm mBEST [5]. This algorithm obtains the centerline coordinates of DLOs within an image by traversing their skeleton pixel representations. The ambiguity of path traversal at intersections is handled by an optimization objective that minimizes the cumulative bending energy of the DLO during the pixel traversal. One case

of extracting discretized patterns from the hand-writing pattern is shown in Fig. 7. RGB images of the deployed DLO are obtained through an Intel Realsense D435 camera as shown in Fig. 9. Further details of the perception algorithm itself can be found in the referenced paper.

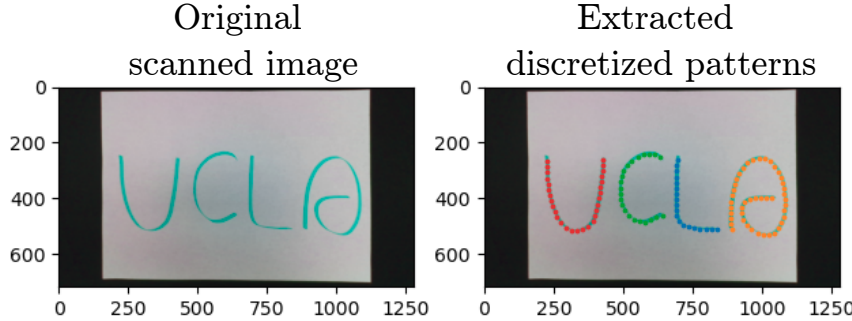


FIG. 7. Scanned handwriting letters and the corresponding extracted discretized patterns.

## B. Motion Planning with the Neural Controller

In Fig. 1, we show the figure which describes the full pipeline of our proposed deployment scheme. Here, we give a full description of how to integrate the trained neural controller into a robot motion planner.

The first step of the deployment process is to specify the desired pattern. This pattern can be defined by either an analytical function or detected as a drawn curve as shown in Fig. 1. Note that the pattern  $\mathbf{P}(s)$  is treated as a function of the curve length  $s$ . Based on the configuration of the pattern, we can compute the required inputs for the neural controller when the connective node  $\mathbf{q}_C$  achieves each point in the pattern  $\mathbf{P}(s)$ . The details of generating an optimal trajectory based on the pattern  $\mathbf{P}(s)$  and the properties of the manipulated rod are given in Alg. 5.

In Alg. 5,  $\kappa$  and  $\mathbf{T}$  are all functions of the arc length  $s$  of the pattern  $\mathbf{P}$  and  $\mathbf{T}$  is the tangent along the pattern. With Alg. 5, we can now obtain the optimal grasp trajectory  $\tau$ , and then use OMPL [37] to generate a valid motion planning sequence.

One highlight of our overall robotic system is its realtime capability. The realtime efficiency of the perception algorithm has been validated by [5] while the average end-to-end time to generate a full optimal deployment motion plan is less than 1 second. Therefore, our

---

**Algorithm 5:** Optimal Deployment Trajectory

---

**Input:**  $\mathbf{P}, L, L_{gb}, \bar{k}_s$ 
**Output:**  $\tau$ 

```

1 Func OPT( $L, \mathbf{P}, L_{gb}, \bar{k}_s$ ):
2    $S, \kappa, \mathbf{T} \leftarrow \text{ProcessPattern } (\mathbf{P})$ 
3    $\Delta s \leftarrow \text{step size of deployment}$ 
4    $\tau \leftarrow \text{initialize an empty list}$ 
5    $\hat{\mathbf{z}} \leftarrow \text{director along vertical direction}$ 
6    $s \leftarrow 0$ 
7    $l_s \leftarrow L$ 
8   while  $s \leq S$  do
9      $\mathbf{q}_C \leftarrow \mathbf{P}(s)$ 
10     $\hat{\mathbf{x}} \leftarrow \mathbf{T}(s)$ 
11     $\bar{\kappa} \leftarrow \kappa(s)L_{gb}$ 
12     $\bar{l}_s \leftarrow (L - s)/L_{gb}$ 
13     $(\bar{\mathbf{q}}_M, \mathbf{e}) \leftarrow \mathcal{F}(\bar{l}_s, \bar{\kappa}, \bar{k}_s)$ 
14     $\mathbf{R} \leftarrow \text{AxangtoRot } ([\hat{\mathbf{e}}, \|\mathbf{e}\|])$ 
15     $\mathbf{R}_t \leftarrow (\hat{\mathbf{x}}, \hat{\mathbf{x}} \cdot \hat{\mathbf{z}}, \hat{\mathbf{z}})$ 
16     $\mathbf{q}_M \leftarrow \mathbf{q}_C + \mathbf{R}_t \bar{\mathbf{q}}_M L_{gb}$ 
17     $\mathbf{R} \leftarrow \mathbf{R}_t \mathbf{R}$ 
18     $\tau.\text{append}((\mathbf{q}_M, \mathbf{R}))$ 
19     $s \leftarrow s + \Delta s$ 
20     $l_s \leftarrow l_s - \Delta s$ 
21 return  $\tau$ 

```

---

approach is also efficient enough to embed into sensorimotor closed-loop control. However, as offline control has achieved excellent deployment accuracy in our experiments, online control is not carried out in this work.

## VI. EXPERIMENTS AND ANALYSIS

### A. Measurement of Material Parameters

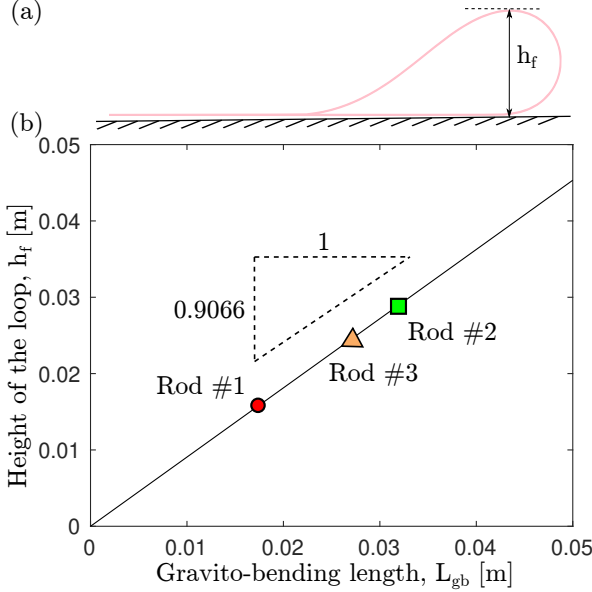


FIG. 8. (a) Deformed configurations of a rod under gravity in 2D plane; (b) Relationship between the height of the loop  $h_f$  and the gravito-bending length  $L_{gb}$ .

To carry out deployment with our proposed scheme, we must validate our experiments with various DLOs. In this article, we choose elastic rods to realize the experiments since elastic rods are canonical examples of DLO, and we can use rapid prototyping scheme to manufacture elastic rods with different material properties so that we can look into the robustness of the proposed scheme against different materials.

First, we need to find the geometric and material properties of the manipulated rod. The geometry of the manipulated rod, e.g., total length  $L$  and rod radius  $h$ , is trivial to measure. Measuring the material properties of the rod is less clear. Overall, we need to develop a way to find the following material properties: gravito-bending length  $L_{gb}$  and normalized stretching stiffness  $\bar{k}_s$ .

Here, we presume the material is linear elastic and incompressible. The incompressible material means the volume of the rod will not change when deformations happen. Therefore, Poisson's ratio is set as  $\nu = 0.5$ . In addition, bending stiffness is  $k_b = \frac{E\pi h^4}{4}$  where  $E$  is Young's Modulus, and the expression for gravito-bending length  $L_{gb}$  and normalized

TABLE I. Material Properties of rods used in experiments

Rod	Material	$L_{gb}$ [cm]	$h$ [mm]	$\nu$	L[m]
#1	Pink VPS	1.8	1.6	0.5	0.875
#2	Green VPS	3.2	1.6	0.5	0.885
#3	Pink VPS	2.86	3.2	0.5	0.84

stretching stiffness  $\bar{k}_s$  is

$$L_{gb} = \left( \frac{Eh^2}{8\rho g} \right)^{1/3},$$

$$\bar{k}_s = \frac{k_s L_{gb}^2}{k_b} = \frac{4L_{gb}^2}{h^2}.$$
(15)

When observing Eq. 15, we find that the only parameter we must obtain is  $L_{gb}$ . It is still unclear how to compute this as  $L_{gb}$  is relevant to Young's Modulus  $E$  and the density  $\rho$  of the rod, which is usually hard to measure. Here, we propose a simple method that is able to measure  $L_{gb}$  by observing the geometry of the rod. When we form a loop in a rod naturally using gravity in a 2D plane, we can observe the geometry of the rod becomes what is shown in Fig. 8(a). Indeed, the height  $h_f$  of the loop has a linear relationship with  $L_{gb}$ . Therefore, we can obtain  $L_{gb}$  for different rods by simply measuring  $h_f$ . According to prior work [28] and our validation shown in Fig. 8(b),  $h_f = 0.9066L_{gb}$ .

In this article, we used two types of silicone-based rubber, vinylpolysiloxane (VPS), to fabricate rods with different material properties. The material and geometric properties of the fabricated rods are given in Table. I. Rods #1 and #2 are used in the experiments of deploying rods along different patterns. For the application of deployment in the knot tying, we used rod #3, which has a larger radius for straightforward grasping for the robot manipulator.

## B. Experiment Setup

For our experiments, we used two Rethink Robotics' Sawyer manipulators as shown in Fig. 9. One arm is attached with a gripper for manipulating the rod. The other arm holds an Intel Realsense D435 camera which is used to scan drawn patterns as well as obtain a top-down view of the deployment result for evaluations.

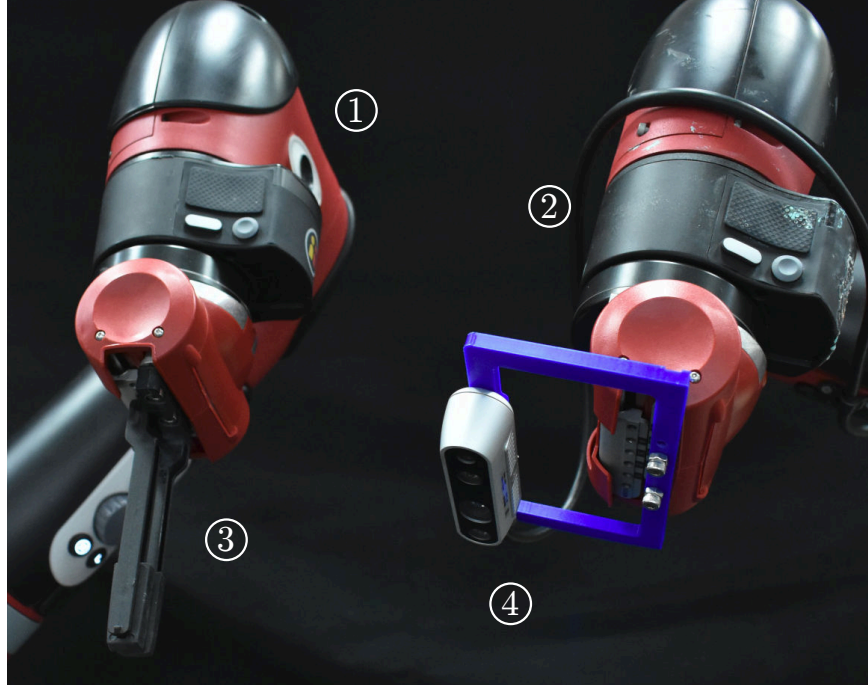


FIG. 9. Experimental apparatus: Two robot manipulators, one for manipulation of the deploying rod (1) and the other for holding the camera for perception (2). A gripper (3) is used for grabbing the manipulated end of the rod. A camera (4) is used for extracting patterns from the drawn patterns and evaluating the deployment results.

In this project, we implement our proposed deployment scheme for three types of tasks. First, we deploy a rod along some canonical cases obtainable through analytical expressions such as a line, circle, and sine curve. The rod is deployed using the robotic arm with the gripper. Once the deployment is finished, the other arm with the camera moves to scan the deployment result. The second task pertains to deploying a pattern that is drawn on a piece of paper. More specifically, the user will draw a pattern on a piece of paper which the camera will then scan to get the ordered discretized pattern coordinates. Afterwards, the robot will manipulate the rod to mimic the drawn pattern on the paper. In this article, we showcase results for drawn “U”, “C”, “L”, and “A” letters. The exact shape of these prescribed patterns are shown in Fig. 10(a). Finally, the last task is to validate the application of the deployment scheme for tying a simple trefoil knot. For this task, both robotic arms are fitted with grippers.

For the first and second tasks, each pattern is evaluated with both the intuitive and

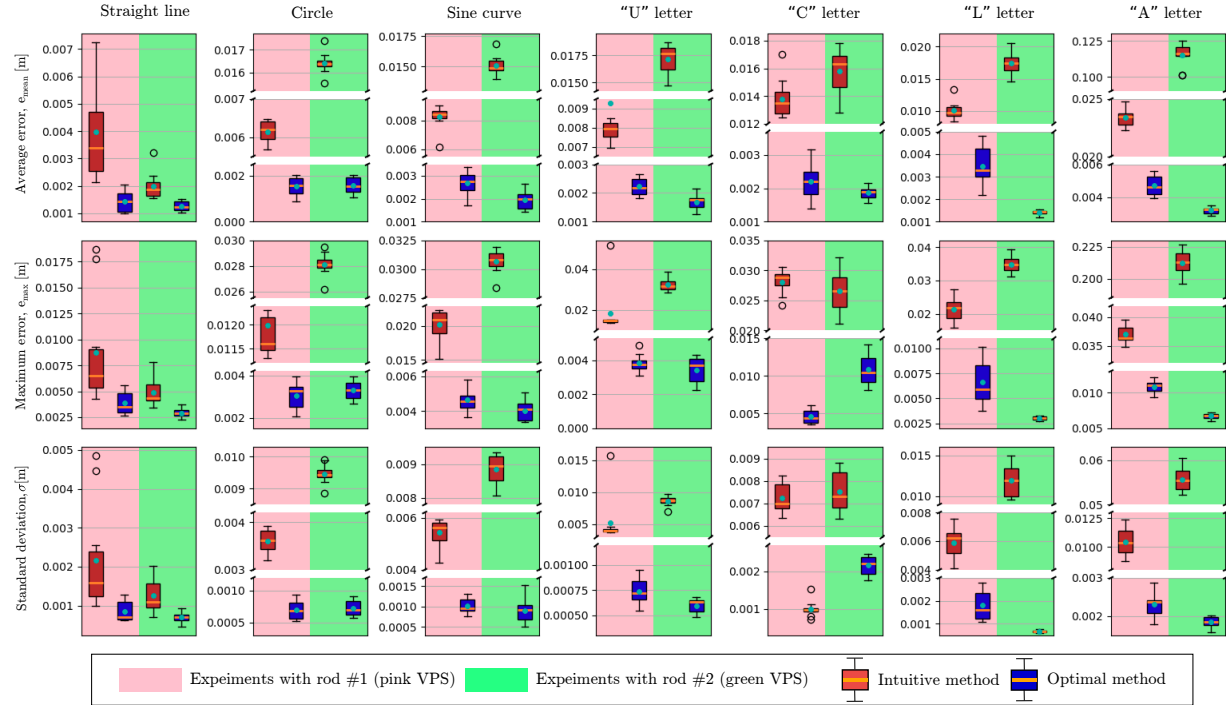


FIG. 10. Experimental results of the deployment results with intuitive and optimal methods. Average error  $e_{\text{mean}}$ , standard deviations  $\sigma$ , maximum error  $e_{\text{max}}$  are shown, and medians are shown as orange lines while means are shown as turquoise circles.

optimal control methods. In addition, two different rods (rods #1 and #2) are used to validate our method's robustness against material differences. For the third task, rod #3 is used for the knot tying task for both algorithms. Each experiment case is tested with 10 trials for each control method. Therefore, a total of 300 experimental trials are conducted for detailed analysis of our deployment scheme's efficacy.

### C. Metrics

We now formulate the metrics used to evaluate the performance of the deployment scheme. When deploying a pattern  $\mathbf{P}$ , we need to assess the accuracy of the deployment result. We first discretize the pattern  $\mathbf{P}$  into  $N$  points and denote the  $i$ -th point of the prescribed pattern as  $\mathbf{P}^i$ . The actual deployment pattern obtained from perception is denoted as  $\mathbf{P}_{\text{exp}}$ . With this discretization scheme, we compute the average error  $e_{\text{mean}}$ , maximum error  $e_{\text{max}}$ ,

and standard deviation  $\sigma$  as

$$\begin{aligned}
e_{\text{mean}} &= \frac{1}{N} \sum_{i=1}^N \|\mathbf{P}_{\text{exp}}^i - \mathbf{P}^i\|, \\
e_{\text{max}} &= \max_{i \in [1, N]} \|\mathbf{P}_{\text{exp}}^i - \mathbf{P}^i\|, \\
\sigma &= \sqrt{\frac{\sum_{i=1}^N (\|\mathbf{P}_{\text{exp}}^i - \mathbf{P}^i\| - e_{\text{mean}})^2}{N}},
\end{aligned} \tag{16}$$

for both the intuitive and optimal control results.

For the trefoil knot tying task, the evaluation of accuracy is not applicable as it is a high-level task. Therefore, we simply use the success rate of the knot tying procedure to evaluate the performance of the deployment scheme. Details of the relevant results and analysis are discussed in next section.

#### D. Results and Analysis

All experimental results can be seen plotted as box plots in Fig. 10. To compute the error metrics in Eq. 16, we used a discretization of  $N = 50$ . In addition to the box plots, a visual comparison is given in Fig. 11. In both figures, an obvious improvement of our optimal control method over the intuitive control method can be observed.

Among the seven deployed patterns, the first three (straight line, circle, and sine curve) are canonical cases, i.e., their shapes have clear analytical expressions. Note that when deploying the circle and sine curve patterns, a small “remainder” section is first deployed. This is necessary as the circle and sine curve patterns have a non-zero curvature at the start of their pattern. We compensate for this by deploying a remainder part whose curvature gradually evolves from a straight line with 0 curvature to the prescribed curvature of the pattern’s first point. The remaining four patterns (“U”, “C”, “L”, and “A” letter cases) do not require this designed remainder. Although these four patterns also have non-zero curvatures at the beginning node of the prescribed patterns, the values of the starting curvatures are not large enough to obviously negatively influence the deployment result.

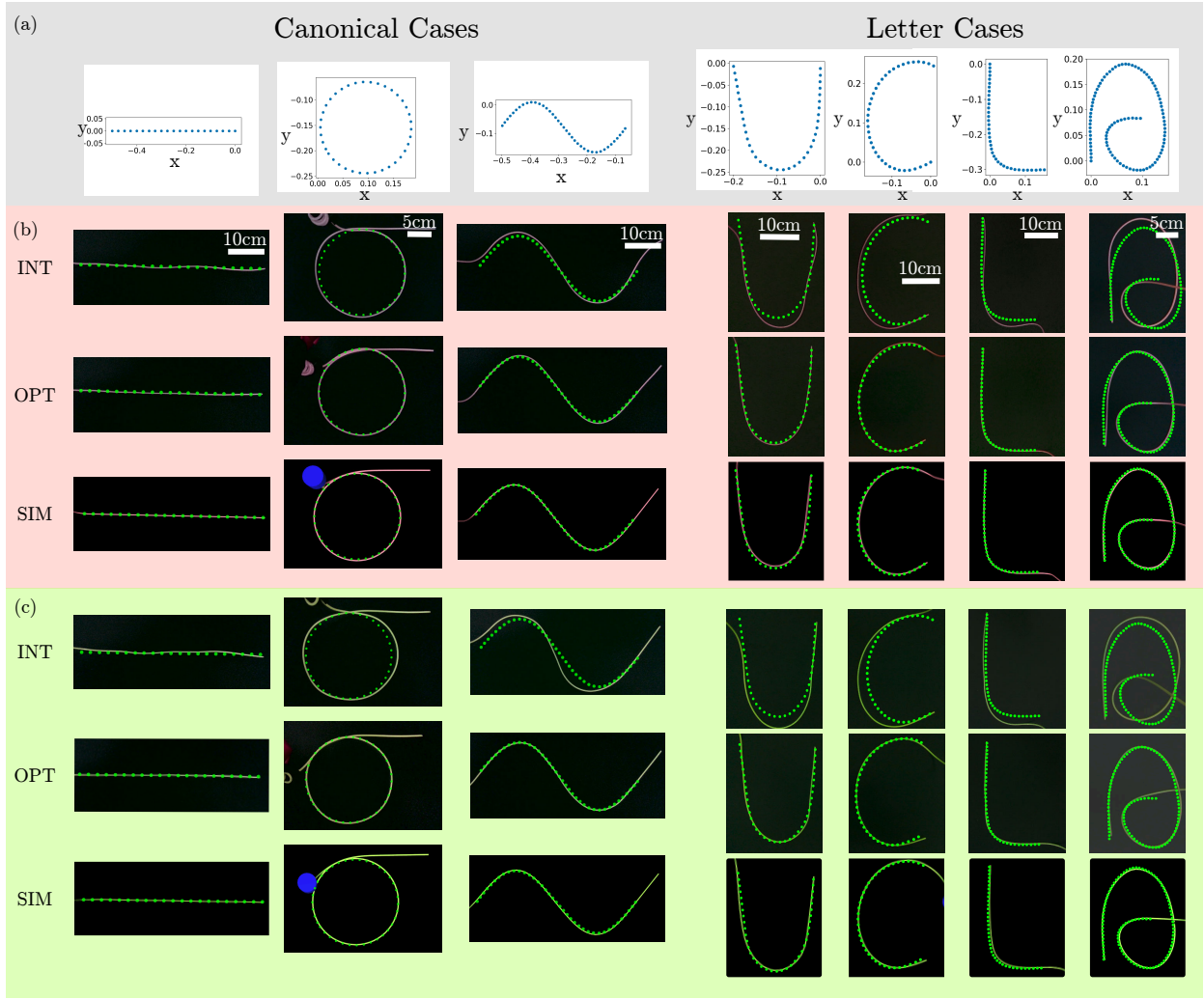


FIG. 11. Experiment results of deployment along various patterns. (a) All used prescribed patterns are discretized and plotted. Deployment results for (b) rod #1 (pink VPS) and (c) rod #2 (green VPS) are shown for each prescribed pattern. Results for the intuitive control method, optimal control method, and simulated optimal control method are shown for each rod.

### E. Tying a Trefoil Knot

Since our optimal deployment scheme can control the shape of a DLO with excellent accuracy, we can use this scheme to tie simple knots. First, the manipulated rod is deployed along a predesigned pattern on the substrate. The predesigned pattern is drawn by users. Then, the camera will scan the drawn pattern and send it to as inputs to our designed scheme. The deployed pattern is designed so that only a simple pick-and-place motion of a single knot segment is required to complete the tying sequence. Since the prescribed pattern's

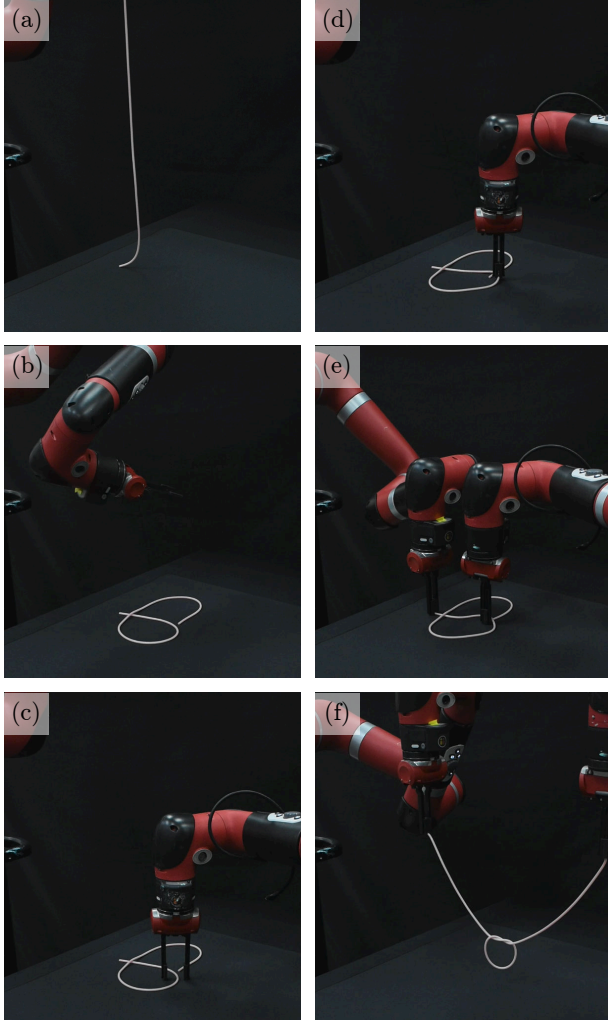


FIG. 12. A demonstration of a trefoil knot tying case using the rope deployment scheme. Time marches from (a) to (f).

shape is known in advance, we can let the robot execute the pick-and-place procedure without perception feedback. So long as the initial deployment is accurate and repeatable, the subsequent pick-and-place procedure should succeed a majority of the time. The knot tying sequence is shown in Fig. 12. For the optimal control method, we achieve a success rate of 90% (9 successful trials out of 10). Based on our observations, the only failure was caused by the rod slipping out of the gripper. In contrast, the intuitive control method achieves a success rate of 0% as the initial deployed pattern does not match the intended pattern. Therefore, the intuitive control method would require some sort of visual feedback to adaptively choose the pick-and-place motion. These results are summarized in Table II.

TABLE II. Trefoil knot tying results

Control Method	Success rate
Intuitive	0/10
Optimal	9/10

## VII. CONCLUSION

In this article, we have introduced a novel deployment scheme that allows for robust and accurate control of the shape of DLOs using a single manipulator. Our framework integrates techniques from various disciplines, including physical simulation, machine learning, and scaling analysis, and has been demonstrated to be highly effective in real robotic experiments. Our results highlight the advantages of incorporating physics into robotic manipulation schemes and showcase impressive performance on complex tasks such as writing letters with elastic rods and tying knots.

Looking to the future, we plan to leverage the precision and efficiency of our deployment scheme to tackle high-level robotic tasks such as knot tying. While exact shape control is not strictly required during such manipulations, our deployment scheme offers sufficient accuracy and efficiency to design the configurations of the middle states of a manipulated DLO, which is essential for robots to successfully tie complex knots. We also aim to explore the use of generalized problem formulations and data-driven control schemes, such as reinforcement learning, to develop more flexible and adaptive solutions to the challenges of robotic manipulation. By continuing to push the boundaries of robotic manipulation, we hope to advance the state-of-the-art in this field and enable new and exciting applications of robotic technology.

**Acknowledgements:** This research was funded in part by the National Science Foundation under award numbers OAC-2209782, CMMI-2101751, CAREER-2047663, and IIS-1925360.

---

- [1] Bergou M, Audoly B, Vouga E, Wardetzky M and Grinspun E (2010) Discrete viscous threads. *ACM Transactions on graphics (TOG)* 29(4): 1–10.
- [2] Bergou M, Wardetzky M, Robinson S, Audoly B and Grinspun E (2008) Discrete elastic rods. In: *ACM SIGGRAPH 2008 papers*. pp. 1–12.
- [3] Buckham B, Driscoll FR and Nahon M (2004) Development of a finite element cable model for use in low-tension dynamics simulation. *J. Appl. Mech.* 71(4): 476–485.
- [4] Choi A, Tong D, Jawed MK and Joo J (2021) Implicit contact model for discrete elastic rods in knot tying. *Journal of Applied Mechanics* 88(5).
- [5] Choi A, Tong D, Park B, Terzopoulos D, Joo J and Jawed MK (2023) mbest: Realtime deformable linear object detection through minimal bending energy skeleton pixel traversals. doi:doi.org/10.48550/arXiv.2302.09444. URL <https://arxiv.org/abs/2302.09444>.
- [6] Clegg A, Yu W, Tan J, Liu CK and Turk G (2018) Learning to dress: Synthesizing human dressing motion via deep reinforcement learning. *ACM Transactions on Graphics (TOG)* 37(6): 1–10.
- [7] Erickson Z, Clever HM, Turk G, Liu CK and Kemp CC (2018) Deep haptic model predictive control for robot-assisted dressing. In: *2018 IEEE international conference on robotics and automation (ICRA)*. IEEE, pp. 4437–4444.
- [8] Geblinger N, Ismach A and Joselevich E (2008) Self-organized nanotube serpentines. *Nature nanotechnology* 3(4): 195–200.
- [9] Guler P, Pauwels K, Pieropan A, Kjellström H and Kragic D (2015) Estimating the deformability of elastic materials using optical flow and position-based dynamics. In: *2015 IEEE-RAS 15th International Conference on Humanoid Robots (Humanoids)*. IEEE, pp. 965–971.
- [10] Haouchine N, Kuang W, Cotin S and Yip M (2018) Vision-based force feedback estimation for robot-assisted surgery using instrument-constrained biomechanical three-dimensional maps. *IEEE Robotics and Automation Letters* 3(3): 2160–2165.
- [11] Jawed MK, Da F, Joo J, Grinspun E and Reis PM (2014) Coiling of elastic rods on rigid substrates. *Proceedings of the National Academy of Sciences* 111(41): 14663–14668.
- [12] Jawed MK, Khouri NK, Da F, Grinspun E and Reis PM (2015) Propulsion and instability of a flexible helical rod rotating in a viscous fluid. *Physical review letters* 115(16): 168101.

[13] Kapusta A, Erickson Z, Clever HM, Yu W, Liu CK, Turk G and Kemp CC (2019) Personalized collaborative plans for robot-assisted dressing via optimization and simulation. *Autonomous Robots* 43(8): 2183–2207.

[14] Kaufmann P, Martin S, Botsch M and Gross M (2009) Flexible simulation of deformable models using discontinuous galerkin fem. *Graphical Models* 71(4): 153–167.

[15] Kita Y, Kanehiro F, Ueshiba T and Kita N (2011) Clothes handling based on recognition by strategic observation. In: *2011 11th IEEE-RAS International Conference on Humanoid Robots*. IEEE, pp. 53–58.

[16] Lee AX, Huang SH, Hadfield-Menell D, Tzeng E and Abbeel P (2014) Unifying scene registration and trajectory optimization for learning from demonstrations with application to manipulation of deformable objects. In: *2014 IEEE/RSJ International Conference on Intelligent Robots and Systems*. IEEE, pp. 4402–4407.

[17] Lee R, Hamaya M, Murooka T, Ijiri Y and Corke P (2021) Sample-efficient learning of deformable linear object manipulation in the real world through self-supervision. *IEEE Robotics and Automation Letters* 7(1): 573–580.

[18] Lv N, Liu J and Jia Y (2022) Dynamic modeling and control of deformable linear objects for single-arm and dual-arm robot manipulations. *IEEE Transactions on Robotics* .

[19] Macklin M, Müller M and Chentanez N (2016) Xpbd: position-based simulation of compliant constrained dynamics. In: *Proceedings of the 9th International Conference on Motion in Games*. pp. 49–54.

[20] Macklin M, Müller M, Chentanez N and Kim TY (2014) Unified particle physics for real-time applications. *ACM Transactions on Graphics (TOG)* 33(4): 1–12.

[21] Maitin-Shepard J, Cusumano-Towner M, Lei J and Abbeel P (2010) Cloth grasp point detection based on multiple-view geometric cues with application to robotic towel folding. In: *2010 IEEE International Conference on Robotics and Automation*. IEEE, pp. 2308–2315.

[22] Matas J, James S and Davison AJ (2018) Sim-to-real reinforcement learning for deformable object manipulation. In: *Conference on Robot Learning*. PMLR, pp. 734–743.

[23] McConachie D, Dobson A, Ruan M and Berenson D (2020) Manipulating deformable objects by interleaving prediction, planning, and control. *The International Journal of Robotics Research* 39(8): 957–982.

[24] Miller S, Van Den Berg J, Fritz M, Darrell T, Goldberg K and Abbeel P (2012) A geometric

approach to robotic laundry folding. *The International Journal of Robotics Research* 31(2): 249–267.

[25] Mitrano P, McConachie D and Berenson D (2021) Learning where to trust unreliable models in an unstructured world for deformable object manipulation. *Science Robotics* 6(54): eabd8170.

[26] Müller M, Heidelberger B, Hennix M and Ratcliff J (2007) Position based dynamics. *Journal of Visual Communication and Image Representation* 18(2): 109–118.

[27] Nair A, Chen D, Agrawal P, Isola P, Abbeel P, Malik J and Levine S (2017) Combining self-supervised learning and imitation for vision-based rope manipulation. In: *2017 IEEE international conference on robotics and automation (ICRA)*. IEEE, pp. 2146–2153.

[28] Pan K, Phani AS and Green S (2020) Periodic folding of a falling viscoelastic sheet. *Physical Review E* 101(1): 013002.

[29] Pignat E and Calinon S (2017) Learning adaptive dressing assistance from human demonstration. *Robotics and Autonomous Systems* 93: 61–75.

[30] Saha M and Isto P (2007) Manipulation planning for deformable linear objects. *IEEE Transactions on Robotics* 23(6): 1141–1150.

[31] Sanchez J, Corrales JA, Bouzgarrou BC and Mezouar Y (2018) Robotic manipulation and sensing of deformable objects in domestic and industrial applications: a survey. *The International Journal of Robotics Research* 37(7): 688–716.

[32] Schulman J, Gupta A, Venkatesan S, Tayson-Frederick M and Abbeel P (2013) A case study of trajectory transfer through non-rigid registration for a simplified suturing scenario. In: *2013 IEEE/RSJ International Conference on Intelligent Robots and Systems*. IEEE, pp. 4111–4117.

[33] Sen S, Garg A, Gealy DV, McKinley S, Jen Y and Goldberg K (2016) Automating multi-throw multilateral surgical suturing with a mechanical needle guide and sequential convex optimization. In: *2016 IEEE international conference on robotics and automation (ICRA)*. IEEE, pp. 4178–4185.

[34] Servin M and Lacoursiere C (2008) Rigid body cable for virtual environments. *IEEE Transactions on Visualization and Computer Graphics* 14(4): 783–796.

[35] She Y, Wang S, Dong S, Sunil N, Rodriguez A and Adelson E (2021) Cable manipulation with a tactile-reactive gripper. *The International Journal of Robotics Research* 40(12-14): 1385–1401.

[36] Stefanidis D, Wang F, Korndorffer JR, Dunne JB and Scott DJ (2010) Robotic assistance im-

proves intracorporeal suturing performance and safety in the operating room while decreasing operator workload. *Surgical endoscopy* 24(2): 377–382.

[37] Sucan IA, Moll M and Kavraki LE (2012) The open motion planning library. *IEEE Robotics & Automation Magazine* 19(4): 72–82.

[38] Sun J, Peng Z, Zhou W, Fuh JY, Hong GS and Chiu A (2015) A review on 3d printing for customized food fabrication. *Procedia Manufacturing* 1: 308–319.

[39] Sundaresan P, Grannen J, Thananjeyan B, Balakrishna A, Laskey M, Stone K, Gonzalez JE and Goldberg K (2020) Learning rope manipulation policies using dense object descriptors trained on synthetic depth data. In: *2020 IEEE International Conference on Robotics and Automation (ICRA)*. IEEE, pp. 9411–9418.

[40] Takizawa M, Kudoh S and Suehiro T (2015) Method for placing a rope in a target shape and its application to a clove hitch. In: *2015 24th IEEE International Symposium on Robot and Human Interactive Communication (RO-MAN)*. IEEE, pp. 646–651.

[41] Tang T, Wang C and Tomizuka M (2018) A framework for manipulating deformable linear objects by coherent point drift. *IEEE Robotics and Automation Letters* 3(4): 3426–3433.

[42] Teo WE and Ramakrishna S (2006) A review on electrospinning design and nanofibre assemblies. *Nanotechnology* 17(14): R89.

[43] Terzopoulos D and Qin H (1994) Dynamic nurbs with geometric constraints for interactive sculpting. *ACM Transactions on Graphics (TOG)* 13(2): 103–136.

[44] Tong D, Borum A and Jawed MK (2021) Automated stability testing of elastic rods with helical centerlines using a robotic system. *IEEE Robotics and Automation Letters* 7(2): 1126–1133.

[45] Tong D, Choi A, Joo J, Borum A and Jawed MK (????) Snap buckling in overhand knots. *Journal of Applied Mechanics* : 1–23.

[46] Tong D, Choi A, Joo J and Jawed MK (2023) A fully implicit method for robust frictional contact handling in elastic rods. *Extreme Mechanics Letters* 58: 101924.

[47] Tong D, Choi A, Terzopoulos D, Joo J and Jawed MK (2023) Deep learning of force manifolds from the simulated physics of robotic paper folding. doi:10.48550/ARXIV.2301.01968. URL <https://arxiv.org/abs/2301.01968>.

[48] Wakamatsu H, Arai E and Hirai S (2006) Knotting/unknotting manipulation of deformable linear objects. *The International Journal of Robotics Research* 25(4): 371–395.

- [49] Wang A, Kurutach T, Liu K, Abbeel P and Tamar A (2019) Learning robotic manipulation through visual planning and acting. *arXiv preprint arXiv:1905.04411* .
- [50] Whitcomb LL (2000) Underwater robotics: Out of the research laboratory and into the field. In: *Proceedings 2000 ICRA. Millennium Conference. IEEE International Conference on Robotics and Automation. Symposia Proceedings (Cat. No. 00CH37065)*, volume 1. IEEE, pp. 709–716.
- [51] Yan M, Zhu Y, Jin N and Bohg J (2020) Self-supervised learning of state estimation for manipulating deformable linear objects. *IEEE robotics and automation letters* 5(2): 2372–2379.
- [52] Yin H, Varava A and Kragic D (2021) Modeling, learning, perception, and control methods for deformable object manipulation. *Science Robotics* 6(54): eabd8803.
- [53] Yu M, Lv K, Zhong H, Song S and Li X (2022) Global model learning for large deformation control of elastic deformable linear objects: An efficient and adaptive approach. *IEEE Transactions on Robotics* .
- [54] Yu W, Kapusta A, Tan J, Kemp CC, Turk G and Liu CK (2017) Haptic simulation for robot-assisted dressing. In: *2017 IEEE international conference on robotics and automation (ICRA)*. IEEE, pp. 6044–6051.
- [55] Zhu J, Navarro B, Passama R, Fraisse P, Crosnier A and Cherubini A (2019) Robotic manipulation planning for shaping deformable linear objects with environmental contacts. *IEEE Robotics and Automation Letters* 5(1): 16–23.